Bulletin of the Seismological Society of America, Vol. 93, No. 3, pp. 1249–1266, June 2003

The 1999 İzmit, Turkey, Earthquake: Nonplanar Fault Structure, Dynamic Rupture Process, and Strong Ground Motion

by Hideo Aochi and Raúl Madariaga

Abstract We simulated dynamic rupture propagation along various nonplanar fault models of the 1999 İzmit, Turkey, earthquake using a boundary integral equation method. These models were inferred from geological and geodetic observations. Based on these results, we modeled seismic-wave propagation around the fault system using a finite difference method. We focused on the effect of different fault geometries on the rupture process and seismic-wave propagation. Numerical simulation results imply a rapid and continuous rupture propagation from the İzmit–Sapanca Lake segment to the Sapanca–Akyazi segment. The rupture under Sapanca Lake appears to have propagated not on a disconnected fault segment but along a smooth fault structure with a bend of only a few degrees. The observational complexity of the surface breaks, however, can be best simulated by a highly segmented fault model. This infers that fault geometric characters observed in the field reflect near-surface structure and that seismological and geodetic features are controlled by global fault structure at depth.

Then we investigated the effect of frictional parameters and the initial stress field. In order to explain near-field seismograms at station SKR, located a distance of a few kilometers from the fault, we had to force the rupture to propagate at shallow depth close to the station. In order to obtain this, we had to introduce a finite cohesive force in the friction law that allows stress accumulation and release in the shallow crust. The external stress field had to be large enough for the rupture to propagate at very rapid speed. Our simulation results show that it is important to include detailed fault geometry in the numerical simulation, and to constrain frictional parameters and the initial stress field, for understanding of the full dynamic process of an earthquake.

Introduction

The 1999 İzmit, Turkey, earthquake (M_w 7.4) occurred on a segment of the North Anatolian fault zone. The surface rupture was well observed (Barka *et al.*, 2000; Lettis *et al.*, 2002) over more than 100 km length, from the Marmara Sea to southwest of Düzce. Barka *et al.* (2002) proposed that it consisted of five segments that, as shown in Figure 1, they named Hersek, Karamürsel–Gölcük, İzmit–Sapanca Lake, Sapanca–Akyazi, and Karadere, from west to east. They observed a maximum right-lateral slip of 5.2 m on the Sapanca–Akyazi segment. Their observations were made only on land; unfortunately, they had no observations under Sapanca Lake or the Marmara Sea. Other geological models propose possible traces of the North Anatolian fault under the lake and the sea (e.g., Arpat, 1999).

Michel and Avouac (2002) used a new technique to process SPOT images that traced the fault with a precision of better than 100 m. This technique revealed a fault geometry much smoother than the ground ruptures mapped in the field (model C in Fig. 1) and a rather smooth distribution of surface fault slip with a maximum slip near Sapanca Lake. Their dislocation model was further constrained from SAR interferometry. These observations suggest that the fault geometric characters observed in the field might inevitably reflect near-surface effects. Wright *et al.* (2001) determined fault orientation and source parameters from interferometric synthetic aperture radar (InSAR) interferometry. Their model (model B in Fig. 1) approximates the observed fault traces on land but implies a fault running under the sea in the western part instead of those observed along the coastline (Barka *et al.*, 2002). Other geodetic analyses also adopted a similar fault system that follows geological observation on the land in the eastern part but remains uncertain under the Marmara Sea in the western part (Delouis *et al.*, 2000, 2002; Reilinger *et al.*, 2000). On the other hand, Bouchon *et al.* (2000, 2002), using a simplified fault model (model A in Fig. 1), determined detailed rupture propagation during the earthquake from the seismic inversion of near-field accelerograms and reported

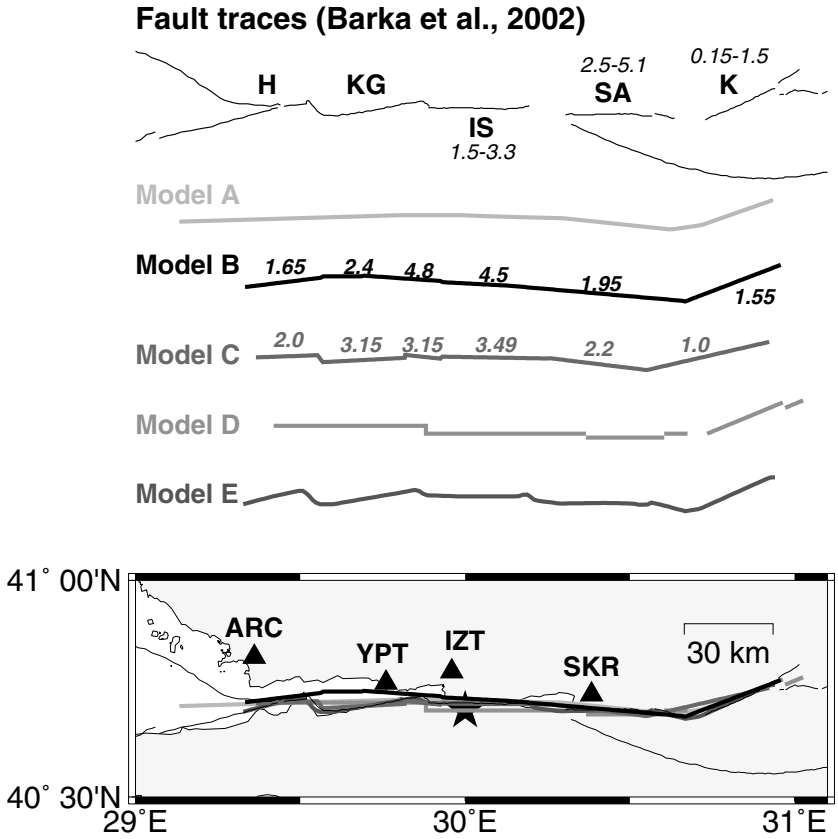

Figure 1. Map of fault models and observed fault traces. From top to bottom: observed fault traces (Barka *et al.* [2002], whose observations results are numbered in meters), fault model A assumed in strong ground motion inversion (Bouchon *et al.*, 2002), fault model B inferred from InSAR geodetic inversion (Wright *et al.* [2001], whose slip model averages from two inversions are shown in meters), fault model C from SPOT image analysis (Michel and Avouac [2002], whose slip model in meters is also shown), fault model D used in the simulation of finite difference method (Harris *et al.*, 2002), and fault model E reflected the observed fault traces shown at the top. At the bottom, we show the position of the fault and the seismic stations. A star represents the epicenter, and triangles show the seismic stations.

that rupture propagated faster in the eastern direction. They found a maximum slip of more than 6 m near the surface to the west of Sapanca Lake. Other seismological inversion results also showed bilateral rupture propagation and a very large slip area near the surface in the western direction (Yagi and Kikuchi, 2000; Sekiguchi and Iwata, 2002). All of these models are very simple and, for example, one planar fault model was adopted (Yagi and Kikuchi, 2000). Many other studies were presented in the special issue of the Bulletin of the Seismological Society of America (February 2002). In any case, the surface observation evidence (Barka *et al.*, 2002; Lettis *et al.*, 2002) is consistent with seismological and geodetic studies of the 1999 İzmit earthquake.

In many of the previous works, the fault models were much smoother than the fault trace observed on the surface (e.g., Fig. 1, models A–C), with the exception of Harris *et al.* (2002), who adopted a disconnected fault system directly inferred from the ground ruptures for testing stress transfer (e.g., Fig. 1, model D). Most of the studies found a series of fault segments with azimuths close to 90° (east–west) from the Marmara Sea to the Akyazi basin and a dipping easternmost Karadere segment with an azimuth of about 70°. Let us consider some of these observations in detail. First, all fault models used in the previous studies (e.g., Wright *et al.*, 2001; Bouchon *et al.*, 2002) bend slightly (a few degrees) under Sapanca Lake, although observations of the fault trace are also compatible with a discontinuous jog, which is smaller than the lake size (a few kilometers). Second, all fault models bend at about 20° in the Akyazi basin, although the basin did not show any surface rupture traces. And, finally, all the models differ significantly in the western part. The fault models determined from InSAR and strong ground motion inversion run along the center of the Marmara Sea, including a few small bends. They seem to extend much further compared to the observed surface traces along the coastline. Their locations are more consistent with the hypocenter distribution of aftershocks (Özalaybey *et al.*, 2002) than with fault-trace observations. The model obtained from SPOT image analysis shows a slightly more complex feature (e.g., Michel and Avouac, 2002). We regard it as an intermediate model between the very complex fault trace observed on land and the simplified fault models inferred from different geodetic and seismic data.

In general, inversion analyses do not have enough resolution to distinguish small differences in fault geometry as seen in Figure 1. However, as shown often, this kind of small-scale fault geometry may affect rupture dynamics significantly. We simulated dynamic rupture process on several different models of fault geometry and investigated their consequences for rupture propagation. The difference in the rupture process due to various fault models necessarily leads to differences in seismic-wave generation. Thus we compare synthetic seismograms with observed near-field ground-motion data to test the different fault models. Finally, we discuss how to constrain the friction law and the initial stress field as well as fault geometry in dynamic modeling of the İzmit earthquake.

Numerical Scheme

For modeling both the rupture process on a nonplanar fault system and the subsequent seismic-wave propagation, we combine two numerical methods: a boundary integral equation method (BIEM) and a finite difference method (FDM). The BIEM is very well suited for dynamic rupture simulation along a nonplanar fault, but it is very expensive to simulate seismic-wave propagation in the earth. On the other hand, the FDM is very suitable for simulating seismic-wave propagation from a kinematic source model, although it is not suitable to treat the rupture process on complex non-coplanar fault geometries. Unfortunately, it is still difficult to calculate the whole process of an earthquake with a single numerical method, such as the finite-element method or the spectral element method, due to technical difficulties. Thus it is convenient and useful to separate the study of the rupture process from that of seismic-wave propagation. We list the numerical parameters used in our simulations in Table 1.

For the numerical simulation of dynamic rupture propagation along nonplanar faults, we use a BIEM for a 3D elastic, homogeneous, unbounded medium (Fukuyama and Madariaga, 1995, 1998; Aochi *et al.*, 2000; Tada *et al.*, 2000). This BIEM is based on boundary integral equations written in terms of stress, removing all strong hypersingularities. This approach has also been used in 2D problems (Cochard and Madariaga, 1994; Tada and Yamashita, 1996, 1997; Kame and Yamashita, 1997, 1999). Since we treat a strike-slip fault that breaks the ground surface, we take care of the effect of the free surface by introducing mirror sources with respect to the surface following Quin (1990), assuming no vertical fault slip. This setting is consistent with the seismic inversion results (e.g., Bouchon *et al.*, 2000, 2002), and the observed horizontal near-field ground motions are actually larger than the vertical ones. We apply this BIEM even for discrete fault model D. We remark that the discrete boundary integral equation is decoupled and can be solved explicitly, independently from the neighboring grids, on each grid and that we do not have any grid between discontinuous steps. This is why the BIEM can treat fault geometry more flexibly. At the beginning of the simulations, we force rupture to propagate at half the speed of the shear wave, until rupture spontaneously propagates at a speed higher than this (Harris and Day, 1999), instead of giving a preexisting finite unstable crack. This is an easy and practical way to start a spontaneous rupture. However we cannot discuss the rupture process in the first 2 sec, nor the initial phase of seismograms, and this process inevitably causes a large slip around the hypocenter (see also Fig. 8). We tested two different grid sizes, 750 and 1000 m, in the BIEM simulation. Since the fault trace is too long to model with the finer grid, we compared the solutions with both grids in their earlier stage, up to 12 sec, and concluded that the coarse grid model was enough to compute seismic-wave propagation.

Based on the rupture history obtained in the BIEM simulation, we compute seismic-wave propagation away from the fault using a FDM. Our FDM is based on fourth-order staggered grids (Virieux and Madariaga, 1982; Olsen *et al.*, 1995; Madariaga *et al.*, 1998) using perfectly matching layers for simulating absorbing boundaries (Collino and Tsogka, 2001). We transform the slip function on the fault computed by the BIEM simulation into a seismic moment distribution computed on each grid point of the FDM simulation (Olsen *et al.*, 2000).

Table 1
Model Parameters

Parameter	Value
Rigidity μ(GPa)	32.4
P-wave velocity V_p (km/sec)	6.0
S-wave velocity V_s (km/sec)	3.54
density ρ (kg/m^3)	2700
Grid size in BIEM simulation Δs (m)	750 (1000)
Timestep in BIEM simulation Δt (sec)	0.06 (0.083)
Grid size in FDM simulation Δs (m)	250
Timestep in FDM simulation Δt (sec)	0.01

Model Parameters

Fault Models

We studied five models with different geometry derived from previous studies of the İzmit earthquake, as shown in Figure 1. Hereafter, we will designate the segmented fault traces between the Hevsek peninsula and Gölcük along the southern coast of the Marmara Sea as segments (H and KG), as well as the segment between İzmit and Sapanca Lake (IS), that from Sapanca Lake to the Akyazi basin (SA), and the easternmost Karadere segment (K) (Barka *et al.*, 2002). As mentioned in the Introduction, we constructed models A, B, and C after Bouchon *et al.* (2002), Wright *et al.* (2001), and Michel and Avouac (2002), respectively. Some segments of the original model were disconnected. However, our reconstructed model is continuous since these irregularities are small compared to the grid size of the simulation. We note that we shortened the original fault model A (Bouchon *et al.*, 2002) at both ends in our simulation so as to make the total fault length similar to the others. Finally, as extreme models, we considered highly segmented models D and E. Fault model D, with several steps and discontinuities, was originally proposed by Harris *et al.* (2002). Although it reflects partially the feature of observed surface breaks, each segment is planar due to numerical constraints in their method. Then we constructed fault model E by scanning the observed fault surface (Barka *et al.*, 2002). We see that fault model D is also a simplified model compared to the complexity of both fault model E and the observed fault trace. In spite of the continuity of fault model E, tectonic stress loading (discussed in the next section) creates negative shear stress accumulation at the short connections between major segments KG and IS, IS and SA, and so on, because the strike

of short connections is in the north–south direction instead of the east–west. This load may cause a left-lateral slip on the connections instead of the right-lateral slip of this earthquake. In this sense, these short connections may disturb the rupture process as much as a barrier and they may play the same role as the steps in fault model D.

The main points we are going to consider are the uncertainty between segments IS and SA under Sapanca Lake, the change in geometry from SA to K, and the different models for the western segments (H, KG, and IS). As summarized in Figure 1, the fault geometry becomes more complex and more segmented from fault model A to E. All the models have a dip of 90° and extend to a depth of 15 km.

Stress Field and Frictional Parameters

In order to define the initial conditions for rupture simulation, we made a simple hypothesis: a uniform external load (remote tectonic stress) is applied over all the rupture area. For the Landers earthquake this approach worked relatively well (Aochi and Fukuyama, 2002). Since the İzmit earthquake is an interplate earthquake and its recurrence time is shorter, the stress field is probably more heterogeneous and affected by the previous rupture history of the fault and by neighboring earthquakes. However, the simple model of uniform external stress should be one of the simplest scenarios among all those that we can imagine. Both the initial stress field and frictional parameters are closely related. We give their detailed mathematical expression in the Appendix.

In our model we let the intermediate principal stress axis be vertical in agreement with a strike-slip fault whose dip is 90°. We determined the direction of the maximum (σ_1) and minimum (σ_3) principal stress axes in the horizontal plane in order for rupture to be most favorable on the primary plane at the hypocenter, that is, on segment IS. This hypothesis is consistent with the movement of the Anatolian plate with respect to the Eurasian plate inferred from Global Positioning System observations (McClusky *et al.*, 2000) and stress analyses in the western North Anatolian fault (Ayhan *et al.*, 2002; Kiratzi, 2002; Polat *et al.*, 2002). Figure 2 summarizes the depth dependence of the assumed principal stress and frictional parameters based on the mathematical expressions of the Appendix. We implicitly include the hydrostatic pore pressure P_H, so that the intermediate principal stress σ_2 corresponds to the effective pressure at all depths, the difference between confining lithostatic pressure P and hydrostatic pore pressure P_H. We take compression as positive, as shown in Figure 3.

We assume a slip-weakening friction law on the fault. The fault strength σ decreases with ongoing slip Δu until a characteristic length D_c is reached:

$$\sigma(\Delta u) = \tau_r + \Delta\tau_b\left(1 - \frac{\Delta u}{D_c}\right) H\left(1 - \frac{\Delta u}{D_c}\right), \quad (1)$$

$$\Delta\tau_b \equiv \tau_p - \tau_r, \quad (2)$$

where τ_p, τ_r, and $\Delta\tau_b$ are called peak strength, residual strength, and breakdown strength drop, respectively. D_c is the critical slip-weakening distance, and $H(\cdot)$ is the Heaviside function. This relation was proposed by Ida (1972) and Palmer and Rice (1973), then observed in laboratory experiments (Okubo and Dieterich, 1984; Ohnaka *et al.*, 1987) and estimated for real earthquakes (Ide and Takeo, 1997; Olsen *et al.*, 1997; Guatteri and Spudich, 2000). In this study, we fixed the slip direction to be everywhere parallel to the fault strike, without a vertical component in agreement with the assumption of principal stresses. In spite of this simplification, it is still difficult to estimate each parameter in the friction law (equation 1). For example, for the 1995 Kobe earthquake, Ide and Takeo (1997) obtained the relation between fault movement and stress during the rupture. Their analysis inferred that the breakdown strength drop $\Delta\tau_b$ was a few megapascals and the critical slip-weakening distance D_c was several tens of centimeters, and it also showed that D_c was a few times longer in the shallow crust (more than 1 m) than in the deeper parts of the fault. However, as they noted, their estimates do not have enough resolution to detect a D_c shorter than 10 cm. Furthermore, Guatteri and Spudich (2000) discussed the difficulties of uniquely determining $\Delta\tau_b$ and D_c. In another analysis, Spudich *et al.* (1998) suggested that absolute levels of stress, that is, τ_p and τ_r, might be a few tens of megapascals, which is much less than those extrapolated from experimental results.

Although this problem is still unsolved, we introduce a depth dependence of friction so that it changes from stable to unstable to stable again with depth, as proposed by Scholz (1988). Considering the previous simulation of the 1992 Landers earthquake (Aochi and Fukuyama, 2002), we first assume peak strength τ_p and residual strength τ_r:

$$\tau_p = \sigma_0 + \mu_s \times \sigma_n, \quad (3)$$

$$\tau_r = \mu_d \times \sigma_n, \quad (4)$$

where μ_s and μ_d are the static and dynamic frictional coefficients and σ_0 is the cohesive force; σ_n is the applied normal stress on the fault. In this simulation, we take into account the time variation of σ_n in equations (3) and (4), although the normal stress change is generally not as large as the shear stress change, and it is small compared to the absolute level of normal stress (Aochi *et al.*, 2002). As a result, the slip-weakening relation in equation (1) is a function not only of fault slip Δu but also of time t, through the normal stress σ_n.

We tried zero cohesive force in preliminary simulations, but we found that it was necessary to introduce a nonzero value in order to explain the large slip observed near the surface (see the Discussion). Thus, in the following simulations, we assume that $\sigma_0 = 5$ MPa. This allows for nonzero stress accumulation on the surface according to equation (A6) of the Appendix, so that there is a finite stress drop at shallow depth. This assumption is qualitatively consistent

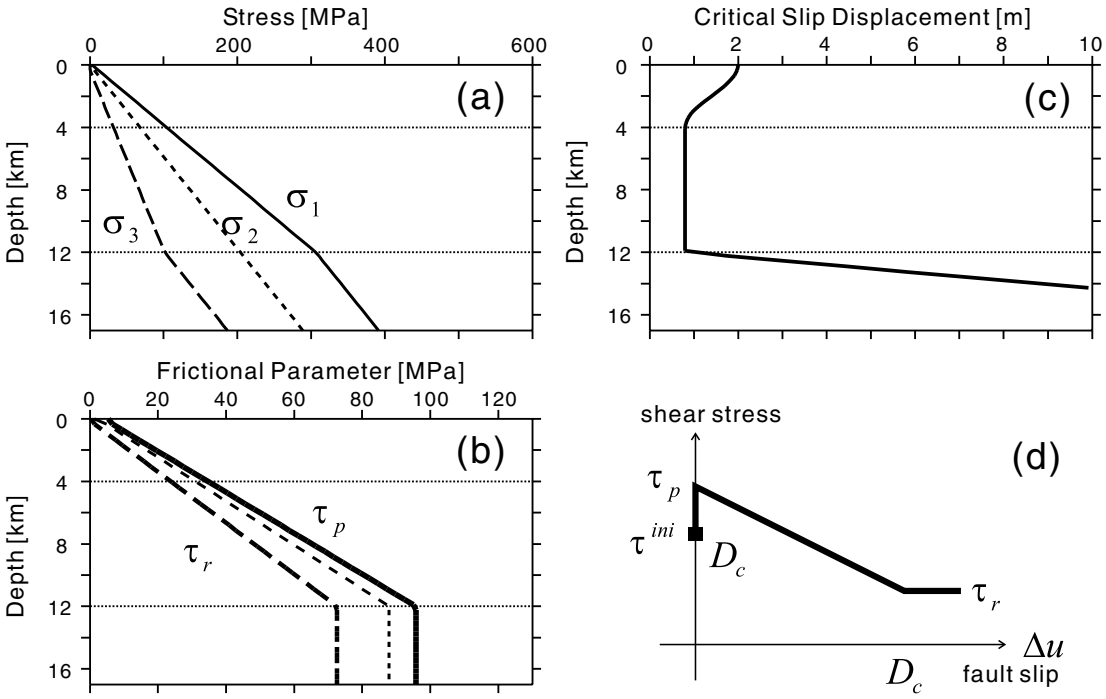

Figure 2. Dependence of stress field and frictional parameters assumed in the reference model for this study ($\mu_s = 0.6$, $\mu_d = 0.48$, $\sigma_0 = 5$ MPa, and $R = 0.66$). See also Figure 3 and the Appendix. (a) Three principal stresses (σ_1, σ_2, and σ_3; $\sigma_1 \geq \sigma_2 \geq \sigma_3$). (b) Frictional parameters on the primary IS segment (peak strength τ_p is the solid line, and residual strength τ_r is the long dashed line). The short-dotted line shows the applied initial shear stress τ^{ini} on the same plane. (c) Critical slip displacement D_c. (d) Illustration of slip-weakening relation of equations (1) and (2).

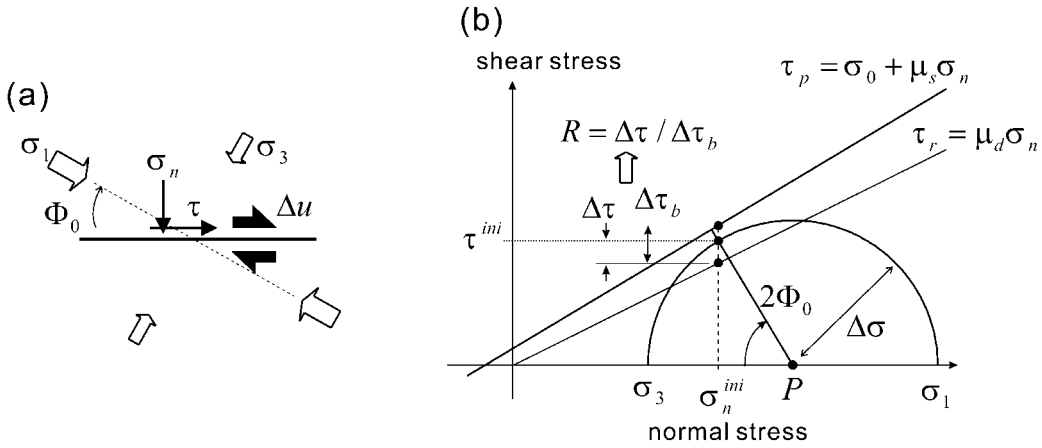

Figure 3. Schematic illustration of the initial situation assumed in the simulations. (a) Relation between maximum and minimum principal stresses σ_1 and σ_3 with respect to the primary plane where the hypocenter is located. (b) Mohr–Coulomb criterion defined for the primary plane. Detailed explanations of each parameter are given in the text and in the Appendix.

with the seismological and geological studies of slip on the fault (Spudich *et al.*, 1998). Figure 2b shows the depth dependency of friction for the first segment IS, assuming $\mu_s = 0.6$ and $\mu_d = 0.48$. Then we introduce the depth dependence of the critical slip-weakening distance D_c as shown in Figure 2c. In order to allow for stable rupture propagation in the shallow crust and at depth, we fix τ_p and τ_r and introduce a longer D_c beneath the depth of 12 km; we also assumed a longer D_c above the depth of 4 km, following our previous work (Aochi and Fukuyama, 2002; references herein).

For given frictional parameters μ_s and μ_d, we can uniquely determine the principal stresses σ_1 and σ_3 with a parameter R (ratio of possible stress drop over breakdown strength drop on the primary plane) as in the Appendix. Since peak strength depends on the normal stress as shown in equation (3), we take the direction of maximum principal stress axis inclined at $\Phi_0 = 29.5°$ from the primary plane corresponding to segment IS after equation (A4) and illustrated in Figure 3a. We give an initial shear stress that is 66% of the breakdown strength drop $\Delta\tau_b$ on the primary fault plane corresponding to segment IS ($R = 0.66$ in equation A5) as in Figure 3b, and hereafter we use this as the reference model whose depth variation appears in Figure 2a. This value preliminary gives a better result among the other values we tried ($R = 1/2$ or 3/4). We remark again that the initial shear stress is nonzero near the surface with nonzero cohesive force σ_0, as clearly inferred in equation (A6), although the lithostatic pressure is zero ($P = 0$). Combination of Figure 2a,b determines the initial stress load at each point on the fault. Figure 4 shows the initial stress for each fault model (A, B, C, D, and E). We note that the condition $R = 0.66$ does not permit rupture propagation on the segment KG and/or SA segment for fault models D and E, because the fault discontinuity or the unfavorably oriented short connection requires much more energy for rupture to jump from the primary segment to the other segment, as often demonstrated in numerical simulations (e.g., Harris *et al.*, 2002). Thus, we had to assume $R = 0.80$ in equation (A5), 21% higher than the previous reference case, in order to get a comparable rupture area and seismic moment release. In all cases, there is always a depth variation of the stress field. The horizontal heterogeneity is clear between different segments rather than within each segment according to fault strike. In the Discussion, we will comment on the sensitivity of different initial conditions on the rupture process and seismic-wave propagation.

Simulation Results

Rupture Propagation

The results of dynamic rupture simulation are compared in the following figures: Figure 5 shows slip velocity snapshots for the different fault models, Figure 6 represents final stress of each simulation, and Figure 7 and 8 show the comparison of numerical simulations with seismological inversion results and with surface break data, respectively. On the whole, we slightly overestimate energy release (M_w 7.6 for models A, B, and D; M_w 7.5 for C and 7.4 for E) compared to the moment magnitude M_w 7.4 (Yagi and Kikuchi, 2000), also seen in the slip distribution and moment release function in Figure 7.

For fault model A, whose geometry is very smooth but includes several small bends, rupture propagates bilaterally on the fault and is very symmetric, as shown in Figure 5a. Toward the east, the main rupture propagates until the large bend and stops there, while some ground surface and shallow crust is fractured on segment K. This partial fracture in the shallow crust comes from its lower level of absolute stress. On the other hand, in the western direction, rupture reaches the end of the fault without any disturbance because there is no significant geometrical irregularity. Finally, we obtain a very uniform final slip distribution and a simple source time function with one peak (Fig. 7). However, we totally over-

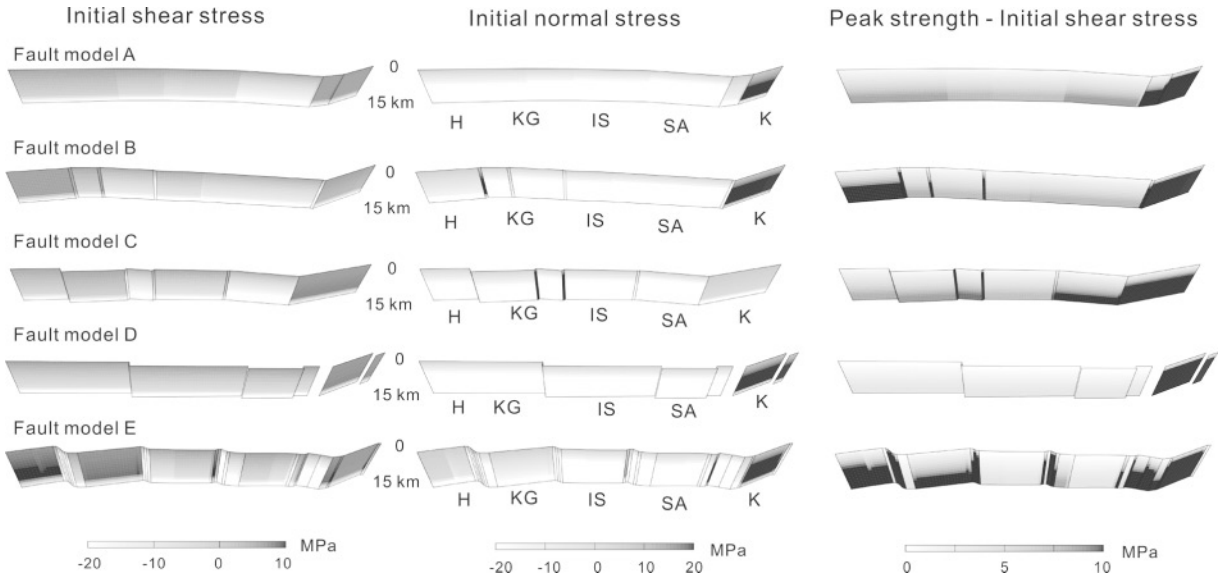

Figure 4. Initial shear and normal stress for each fault model (A, B, C, D, and E). The values are deduced based on $\mu_d \times$ effective pressure ($P - P_H$) and effective pressure ($P - P_H$), respectively. The right panel shows the difference between peak strength τ_p and initial shear stress τ^{ini}.

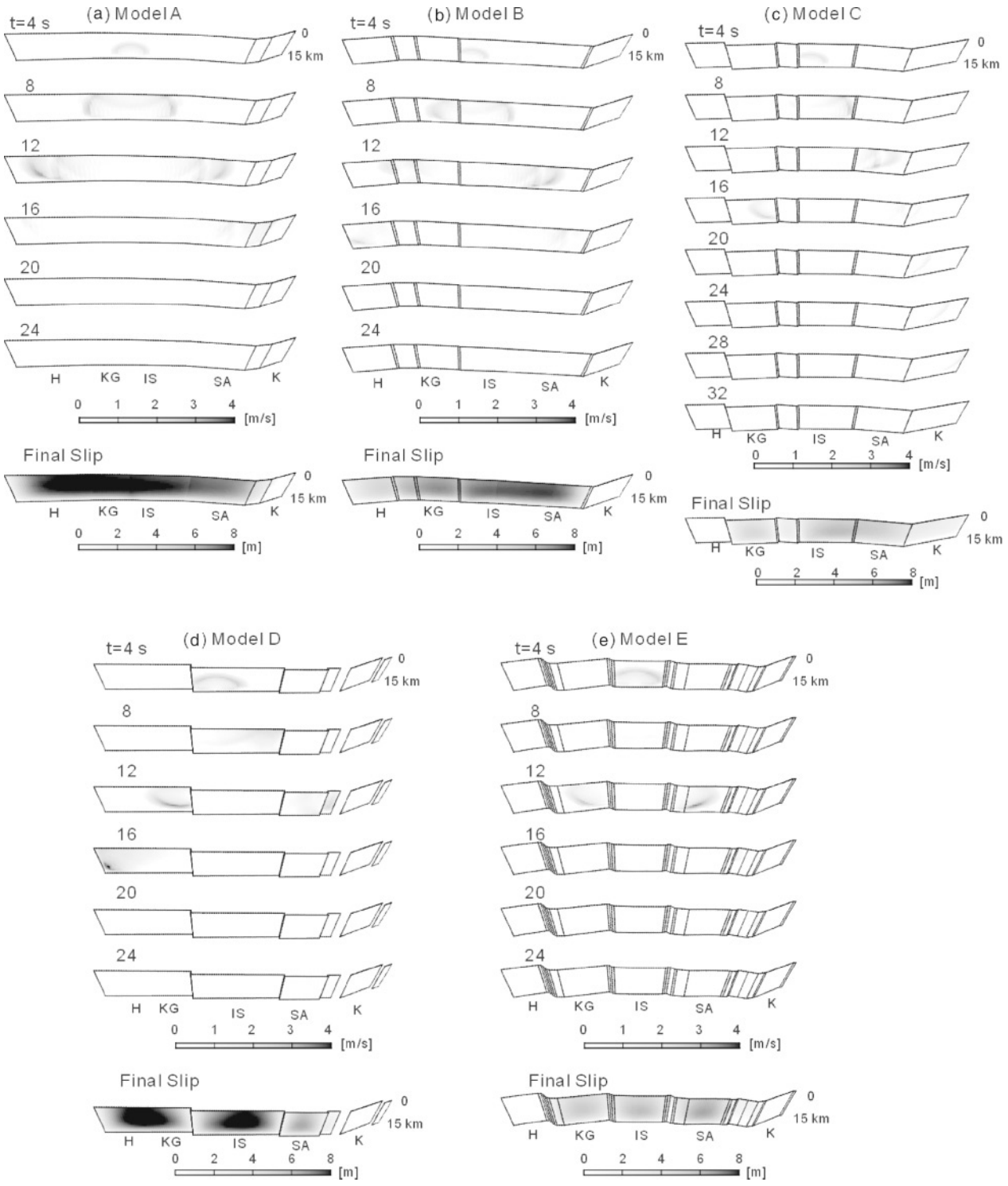

Figure 5. Snapshots of dynamic rupture simulations for different fault models. (a) Fault model A, (b) model B, (c) model C, (d) model D and (e) model E illustrated in Figure 1. The upper snapshots represent the history of slip velocity on the fault. The bottom ones show the final slip distribution.

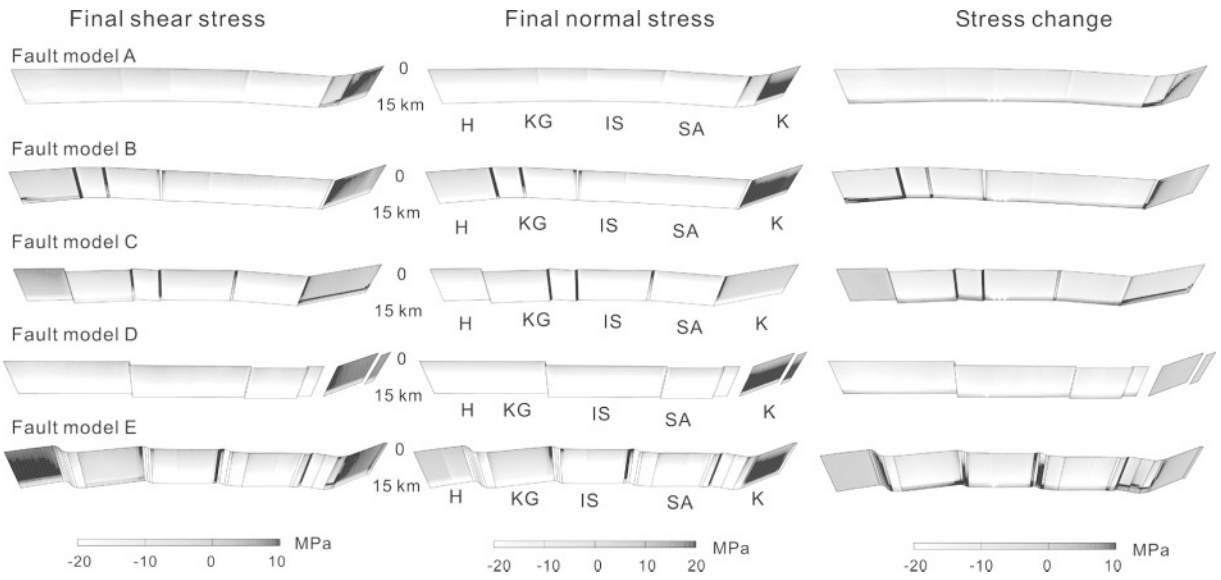

Figure 6. Final shear and normal stress for each of fault models A, B, C, D, and E. The values are reduced in the same way as in Figure 4. The right panel shows the change of shear stress on the fault.

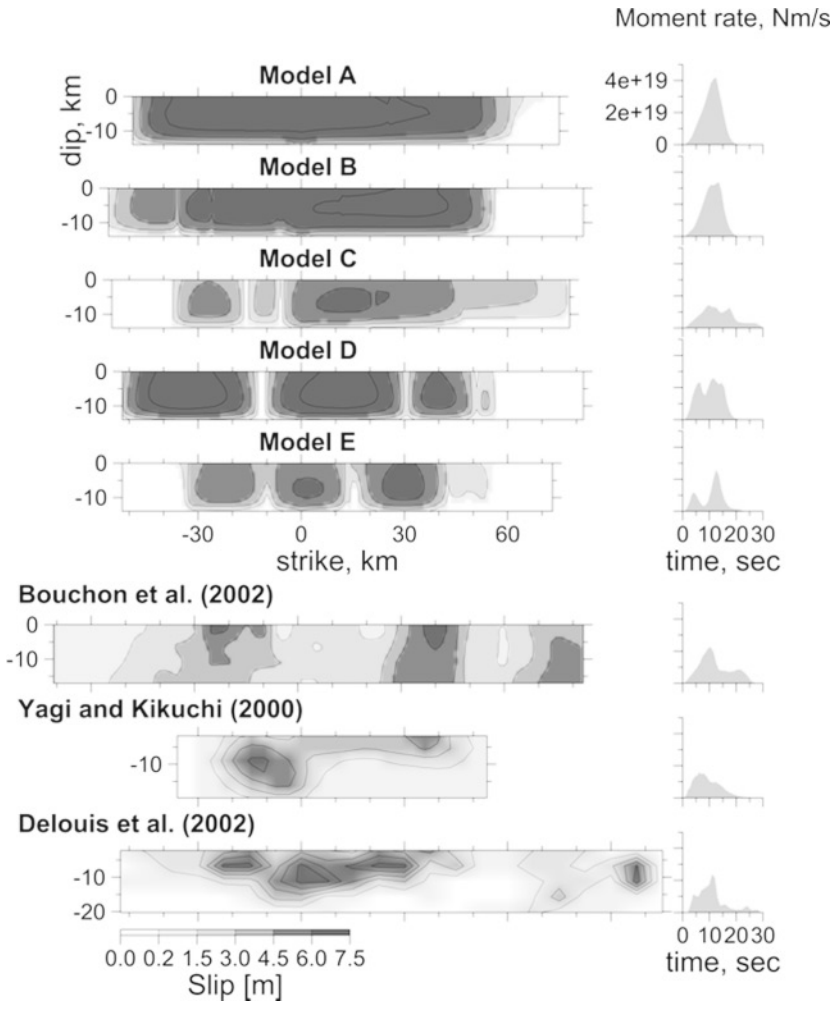

Figure 7. Comparison of each model and seismic/combined inversion results (Yagi and Kikuchi, 2000; Bouchon *et al.*, 2002; Delouis *et al.*, 2002). The left column is the final slip distribution, and the right shows each source time function.

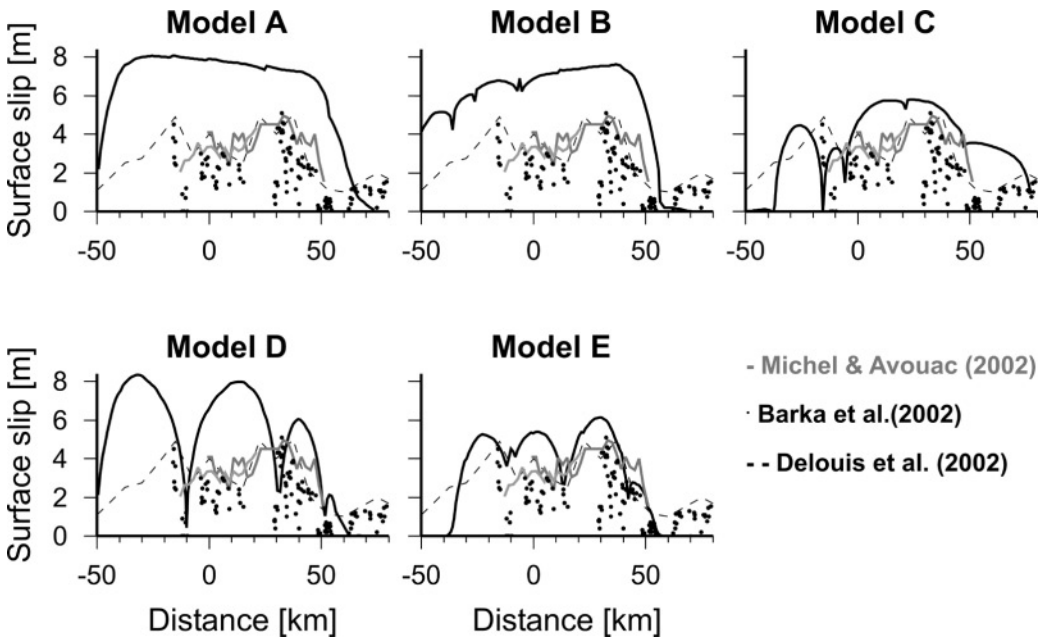

Figure 8. Comparison of synthetic ground break for each model. The origin of strike is taken to the hypocenter. Analysis results of SPOT images (Michel and Avouac, 2002) are simultaneously shown as two gray lines, and the slip distribution at the shallowest subfault in the combined inversion (Delouis *et al.*, 2002) is also shown as a dashed line. Black circles represent observed surface breaks (Barka *et al.*, 2002).

estimate their values, as also observed in surface break displacement (Fig. 8), because of the smoothness of this fault model.

Fault models B and C, shown in Figure 5b,c, involve small irregularities, particularly in the western part of the fault. In both models, rupture propagates initially toward the east and, after a small delay, it begins propagating westward. Since fault model C has a more complex geometry, it produces a complex stress heterogeneity as shown in Figure 4, and westward propagation is more complex and slower. The strike of the easternmost segment, K, is slightly different from that of the main fault. As a result, rupture is arrested there in fault model B, whose bending angle is larger, but it continues to propagate with slow rupture speed until the end of the fault in model C. We observe clear differences in the stress distribution on segment K: in Figure 4, higher initial shear stress and lower initial normal stress for model C. These differences appear in the source time function, too. Model C has a slow acceleration and a long duration. In conclusion, fault slip becomes more heterogeneous and smaller as fault geometry becomes increasingly complex from models A to C in Figures 7 and 8.

Fault model D, on the other hand, shows quite different features, as seen in Figure 5d. Rupture propagates initially just on segment IS and, after a while, it suddenly transfers to the neighboring segments, KG and SA. Rupture propagation seems to be very intermittent, although the different parallel segments of this model are under the same initial stress condition (Fig. 4). The reason for the delays is that the rupture front does not propagate continuously, so that stress concentration on the second segment takes a longer time to build. This feature is clearly observed in Figure 7. We see two main concentrations of moment release in time. Each moment release occurs very rapidly and maximum slip is very large, because we impose higher stress accumulation in order for rupture to jump to each of the successive segments. These main features of rupture propagation seem to be the same as in the previous FDM simulation by Harris *et al.* (2002), although they did not show any detailed snapshot or slip distribution of rupture propagation. The main difference between their model and ours is in the different stress conditions and frictional parameters, particularly in that we introduce a depth-dependent friction proportional to the confining pressure of the crust. As a result, it becomes difficult to create a large slip in the shallow crust where stress release is always smaller than at depth, as further discussed in the Discussion. On the other hand, in the case where one supposes a uniform frictional behavior, it is easy to create a large slip in the shallow crust enhanced by the effect of the surface (e.g., Harris and Day, 1999; Harris *et al.*, 2002).

The different features that appear in fault model D become clearer for fault model E. The rupture pattern involves multiple shocks, as seen in the snapshot (Fig. 5e) and in the moment release rate (Fig. 7). Slip distribution is strongly controlled by the segmentation, as also observed in Figure 7.

Seismological inversion results (e.g., Bouchon *et al.*, 2002; Yagi and Kikuchi, 2000; Delouis *et al.*, 2002) infer

mainly two asperities at 30–40 km east and at 10–30 km west of the hypocenter. Comparing the simulation results (Fig. 7), those corresponding to segments KG and SA are very roughly simulated in the numerical models (fault models B, C, D, and E). In particular, the appearance of the eastern asperity on or near the surface in all inversion results infers a finite stress drop in that region, and this is realized in the numerical simulations under the condition of finite cohesive force σ_0 permitting a finite stress accumulation and drop. The simulation results show another asperity around the hypocenter on segment IS for fault models C, D, and E, although it is not localized well for fault models A and B because of the smoothness of their fault geometry. The existence of this asperity is inferred from other inversion results (e.g., Delouis *et al.*, 2000; Reilinger *et al.*, 2000). On the other hand, the seismic moment release rate (Fig. 7) gives us a simple rupture process with one peak around 7–10 sec and a duration of 15–20 sec (fault models A, B, or C). The long duration after 20 sec comes from the rupture on segment K (fault model C; Bouchon *et al.*, 2002).

From the geodetic viewpoint, fault model C shows similar surface breaks to the result of the analysis of SPOT images (Michel and Avouac, 2002) and the slip distribution at the shallowest subfault in the combined inversion result (Delouis *et al.*, 2002). The trend of their analyses also appears in fault model B, in spite of a discrepancy in the values. On the other hand, geological observations of surface breaks (Barka *et al.*, 2002) are more consistent with fault model E. In general, as seen in the slip distribution of Figure 7, surface breaks are strongly controlled by fault segmentation as well as asperities. As the fault geometry becomes more complex from model A to E, surface breaks show more complexity. Furthermore, the degree of segmentation may determine the maximum amount of surface breaks on each segment, as a larger and smoother segment produces larger surface breaks.

Based on all these considerations, among the five different fault geometry models, fault models B and C explain the seismological data better. We observe rapid rupture propagation in the eastward direction on segments IS and SA until the large bend. This fast rupture propagation is a consequence of the smooth fault geometry there. Therefore, under Sapanca Lake, the change in fault geometry may be very small. Fault bends probably exist also under Sapanca Lake, but they may not be large enough to play the role of a barrier for rupture propagation. Segment K is very sensitive for rupture propagation. Far-field waveform inversion by Yagi and Kikuchi (2000) suggested an arrest of rupture around this bend, but strong ground motion data at a further eastern station not shown in Figure 1 and geodetic data imply that there was some slip on segment K (e.g., Bouchon *et al.*, 2000, 2002; Delouis *et al.*, 2000, 2002; Wright *et al.* 2001). We observe that rupture propagates slowly on segment K of fault model C and that it leaks into the shallow crust in fault model A (Fig. 8), whereas it is arrested around the bend in fault model B. The reason that these different behaviors of fault segment K occur in numerical modeling is that rupture along this segment is not favored with respect to the initial stress field. On the other hand, rupture propagation is slower in the western direction compared to the eastern side. This implies that the complexity of the inferred fault geometry in the western part of the fault strongly affects the propagation of rupture.

Seismic-Wave Propagation in the Vicinity of the Fault

From the rupture history on the fault system computed in the previous section, we can simulate seismic-wave propagation using the FDM. Figure 9 shows snapshots of propagation for two different fault geometry models (B and E). We observe that large amplitudes of ground motion are generated by the passage of the rupture front. Disturbances of rupture due to fault segmentation also cause strong waves that look like stopping phases. This is why fault model E produces more complex wave generation. Figure 10 shows comparisons of synthetic and observed seismograms at the strong ground motion stations shown in Figure 1. Since the spatial grid of the BIEM for rupture simulations is presently 1 km, the resolution of seismograms is several times this grid size. For this reason we low-pass filtered observed ground displacements at 1 Hz.

None of our fault models can exactly explain the observed seismograms because we assumed a very simple initial stress and a laterally uniform friction law. In spite of this limitation we find many characteristic features of the observed records in our models. Station ARC is the farthest from the rupture of the four stations. Fault models A and D have too large an amplitude in the horizontal components compared to the other models. That is because both models overestimate the seismic moment and produce too much amplitude, especially in the western segment of the hypocenter. As we stated in the previous section, fault model B fits the observed data better than the other models. Fault models C and E produce several pulses in the north–south component, unlike the observations, which reflects an intermittent or very slow westbound rupture process.

At station YPT, on the other hand, synthetic seismograms for models A, B, D, and E reproduce the first signal accompanying rupture passage, and we recognize some later phases. The splitting of waveforms observed in fault model A is due to an extremely fast rupture propagation. As the rupture speed becomes faster than the shear wave speed, the rupture front splits into two parts, as seen in Figure 5a. One of them propagates at a speed faster than the shear-wave speed, while the other one progresses at the Rayleigh wave speed. The origin of multiple pulses generated at station YPT in fault models D and E is different. Since the fault segments are segmented in these models, rupture proceeds as a series of multiple disjoint shocks as observed in Figure 5d,e and shown by the moment release rate in Figure 7. Our velocity model is very simple, and we cannot completely exclude some complexity in the observed waveforms that may come from wave propagation in a heterogeneous medium rather than from a complex rupture process. Our simulations

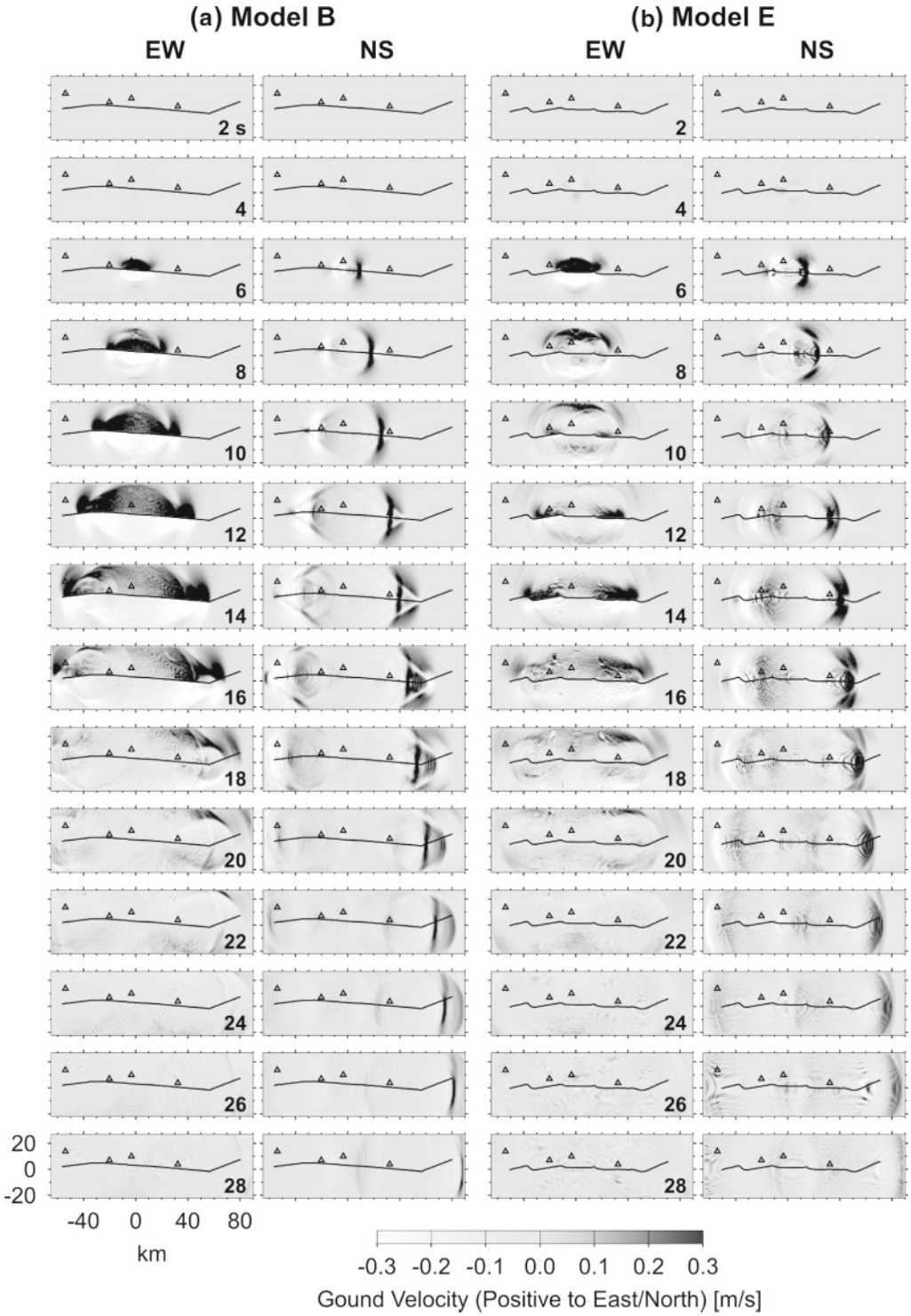

Figure 9. Snapshots of simulations of seismic-wave propagation using the FDM. They show the velocity of the ground motion in the east–west and north–south directions. Triangles show the location of seismic stations, and solid lines represent each fault model. The columns correspond to (a) fault model B and (b) model E following the simulation of Figure 5.

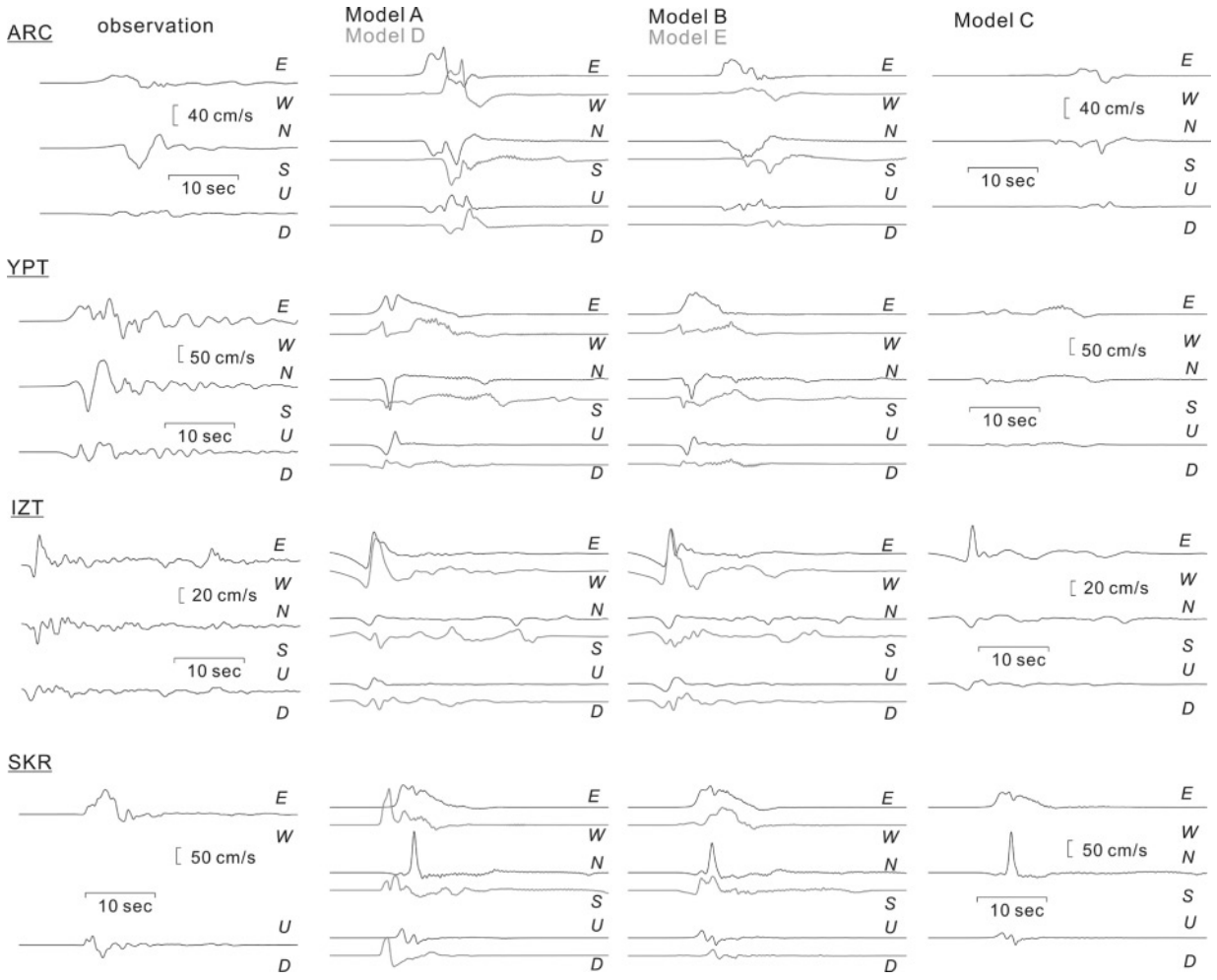

Figure 10. Comparison of observed (left column) and synthetic seismograms for all fault models (A, B, C, D, and E). In each panel, we show velocity waveforms in the east–west, south–north, and up–down components, from top to bottom. The seismograms are low-pass filtered with corner frequency 1 Hz, except those for station IZT, which are zero-phase bandpass filtered between 0.07 and 1 Hz.

clearly support an important role for complex fault geometry as in fault model B or other more complex models with variable stress and friction.

We need to be much more careful in comparing observed and simulated seismograms at station IZT close to the hypocenter. This is because we begin all the simulations of rupture propagation by forcing initial rupture at constant speed until rupture propagates spontaneously. This corresponds to the first 2 sec, and by that time, the rupture area has reached a size of 3 km. This is why we generate very similar waveforms in all our models.

Finally, let us analyze records at station SKR, located just a few kilometers from the fault trace. The observation shows a simple envelope of about 80 cm/sec maximum velocity and a pulse width less than 10 sec in the east–west component. This implies a very simple rupture passage by the station. This feature is reproduced well by fault models A, B, and C, where the fault plane is very smooth and allows continuous rupture propagation as seen in Figure 5. The multiple pulses generated by fault models D and E are due to the same cause as those at station YPT, although the first signal is very weak for fault model E. It is due to the sudden arrest and subsequent jump of rupture from the IS to the SA segment.

Discussion

Indication from Near-Field Seismograms

Bouchon *et al.* (2000) reported that a simple Haskel model can explain very well the observed seismograms at stations ARC and SKR. They found a westbound rupture velocity of 3 km/sec (for ARC) and an eastbound speed of 4.7 km/sec (for SKR). Their result also supports a smooth fault geometry in the eastern direction on which rupture can rapidly propagate as in our fault models A, B, and C. The syn-

thetic seismograms based on dynamic rupture simulation do not fit the observations as well as the simple kinematic model estimated by Bouchon *et al.* (2000). We observe that the slip pulses generated by our simulations (Fig. 5) are not as simple as those produced by a simple kinematic Haskel model. The reason is that our simulation takes into account a 3D fault model with heterogeneous frictional parameters and a free surface, a situation similar to that modeled by Aagaard *et al.* (2001). In our simulations, rupture propagates not only in the strike direction but also vertically. We observe that rupture progresses more rapidly near the surface and recognize a downgoing rupture phase from the surface. Furthermore, we also found that the rupture front tends to split, so that the total duration of the slip pulse is long. These are consistent with the simulation of Aagaard *et al.* (2001). Therefore the rupture process in the numerical simulations is more complex than the Haskell model introduced by Bouchon *et al.* (2000). Thus an important question is why the real rupture process of this earthquake was so simple and which of the model parameters controlled that feature.

Here we try changing the details of rupture front propagation, especially in the eastern direction, by modifying the frictional parameters or the initial stress level. We adopt model B for the fault geometry and compare seismograms at stations ARC and SKR. First, let us consider the effect of the cohesive force σ_0 in equation (3). Figures 11b and 12b show a snapshot of rupture propagation and a comparison of seismograms in the case of $\sigma_0 = 0$, respectively. We see that the rupture propagates preferentially at depth, whereas it propagated near the surface in the case of $\sigma_0 = 5$ MPa, as shown in Figure 5b and illustrated again at the left column of Figure 11. That is why we do not see any large slip on and near the surface in the final slip distribution. This is not consistent with observational or inversion results (e.g., Yagi and Kikuchi, 2000; Bouchon *et al.*, 2002; Delouis *et al.*, 2002). Furthermore, the synthetic seismograms are quite different. At station SKR very close to the fault, the pulse width is much longer and its amplitude smaller, because rupture propagated at depth. Thus our numerical experiment clearly implies the existence of a finite cohesive force near the surface. This means, in other words, that there is some finite fault strength on the surface even if the lithostatic pressure is zero there. This is the only way to allow for stress accumulation and release on and near the surface, so that large slips can be produced in the shallow crust. We remark that this is a common feature we also found in the simulation of the 1992 Landers earthquake (Aochi *et al.*, 2003). This feature may be intrinsic in the fault behavior of strike-slip faults. Observations at station ARC are not clear enough to discuss this problem. The main phase of the seismogram is delayed, because the rupture process is disturbed due to the irregular fault geometry just west of the hypocenter. Also, since the station is located far from the fault, we do not see any characteristic feature in the seismograms.

Next we try to control the rupture velocity. In fact, the rupture velocity seen for fault model B (Fig. 5b and the left of Fig. 11) is faster than the shear-wave speed. In order to reduce rupture velocity, we suppose here that the initial stress level is 50%, 24% lower than the reference case, with respect to the breakdown strength drop $\Delta\tau_b$ on the primary fault segment IS ($R = 0.50$ in equation A5). We also reset $\sigma_0 = 6.6$ MPa and $\mu_d = 0.44$, in order to get a comparable seismic moment to the previous case. Briefly, we modify the initial stress field in order to conserve the potential stress drop (or the available strain energy) on the primary plane. Figures 11c and 12c show snapshots of rupture propagation and synthetic seismograms. It is well known that it is very easy to create both supershear and sub-Rayleigh rupture fronts, as many numerical simulations have shown since the study of Das and Aki (1977). In the case of slow rupture velocity (Fig. 11c), the rupture front does not split and the slip pulse is very narrow. Although the pulse width of the seismogram becomes slightly longer at station SKR, it may be still possible to create similar waveforms. Although the westbound rupture initiation is delayed for the first 7 sec because of the fault irregularities located to the west of the hypocenter, we can discuss the later part of the westward rupture propagation, which affects seismic-wave propagation. In fact, we observe that the synthetic seismograms at station ARC explain well the observed one. The movement of the rupture front is similar to the inversion result of Sekiguchi and Iwata (2002).

All our simulation results show systematically a longer pulse width of seismograms at station SKR, due to a longer duration of the slip pulse on the fault. Another possible scenario we can propose for shortening the pulse width is that the maximum fault depth may be shallower than inferred from the inversion result of Yagi and Kikuchi (2000), although the distribution of aftershocks extends down to 15 km depth (Özalaybey *et al.*, 2002) and other inversion results require fault slip at depth (Bouchon *et al.*, 2000, 2002). Otherwise, there may be some mechanism of rapid healing that we did not include in the frictional law as originally proposed by Heaton (1990) and as shown numerically by Cochard and Madariaga (1994) and Nielsen and Olsen (2000) and analytically by Nielsen and Madariaga (2003).

Heterogeneous Stress Loading

What our simulations lacked is the previous history of this fault system. For this reason, we assumed a uniform external load for determining applied initial stress on the fault system. It is clear that this assumption is not correct, particularly near both ends of the fault, because they must be affected by the residual stress field from previous events. In fault models A, B, and D (Fig. 5), the westbound rupture stopped at the end of the fault model. The western termination may be affected by the complexity of fault geometry under the Sea of Marmara and also by the history of previous events. Unfortunately we did not implement any method to take into account this information quantitatively in numerical simulations.

Hashimoto and Matsu'ura (2002), for example, studied

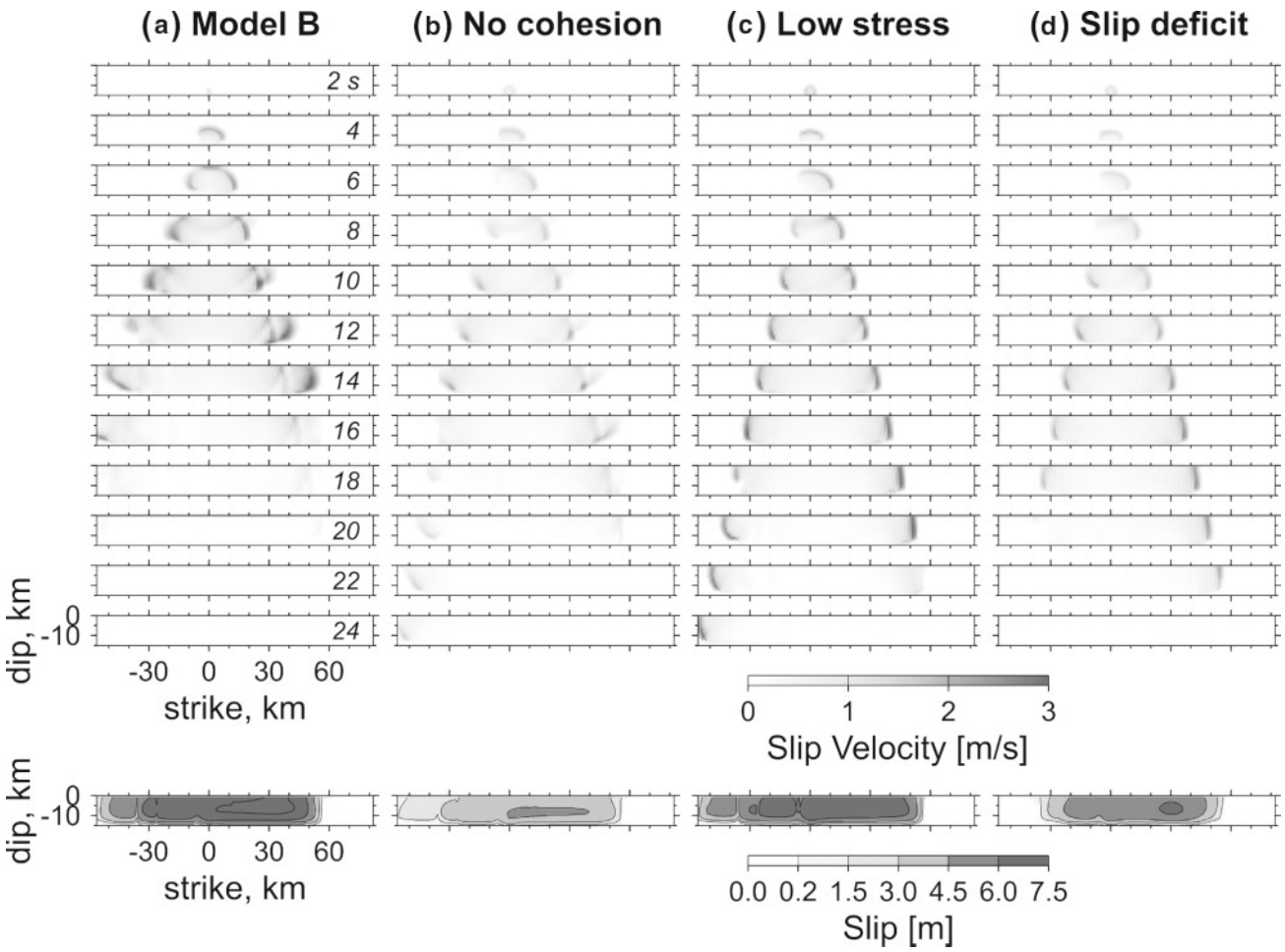

Figure 11. Comparison of dynamic rupture propagation on fault model B for different scenarios. (a) The reference simulation already shown in Figure 5(b). (b) The case of no cohesive force ($\sigma_0 = 0$ MPa), (c) slower rupture velocity under low stress accumulation ($R = 0.5$), and (d) heterogeneous stress loading considering previous history (Fig. 13).

a quasi-static simulation of inter-seismic fault slip until the instability of dynamic rupture. They included a tectonic loading function, viscoelastic structure, and a slip- and time-dependent friction law, but the fault is one planar strike-slip segment. Even for that case, they showed that stress concentrates in a complex way on the segment due to the interaction between all factors. On the other hand, Stein *et al.* (1997) and Reilinger *et al.* (2000) calculated stress change along the North Anatolian fault produced by a series of earthquakes. It is reasonable that stress concentrates in the seismic gaps, but the change of stress is usually smaller than 0.1 MPa. Compared to the average stress drop of a few megapascals, this stress change is negligible for numerical simulation of dynamic rupture. This is because their estimation lacks the effect of a tectonic steady loading and viscoelastic asthenosphere. If possible, it would be a correct way to model the whole quasi-static process including fault geometry, tectonic loading, fault interaction (event history), and visco elastic asthenosphere, in order to quantitatively obtain the stress condition just before the instability of dynamic rupture (Fukuyama *et al.*, 2002).

Here, we propose an alternative method for our simple loading system σ_1 and σ_3 in order to include the effect of previous events. Hubert-Ferrari *et al.* (2000) and Barka *et al.* (2002) studied a series of earthquakes along the North Anatolian fault during the last 300 years. It is clear that the ruptures of August and November 1999 occurred in areas of slip deficit. We transform this 1D information (figure 19B of Barka *et al.*, 2002) in a quantitative way. For a 2D in-plane static problem, shear stress τ due to a discontinuity Δu on a crack Σ is given by

$$\tau(x) = -\frac{\mu}{2\pi}\frac{1}{1-\nu}\int_{\Sigma}\frac{1}{x-\xi}\frac{\partial}{\partial\xi}\Delta u(\xi)\mathrm{d}\xi, \qquad (5)$$

where x and ξ represent positions along the crack and ν is the Poisson ratio. Figure 13 shows the simplified slip deficit $\Delta u(\xi)$ and the resultant stress $\tau(x)$ following from equation

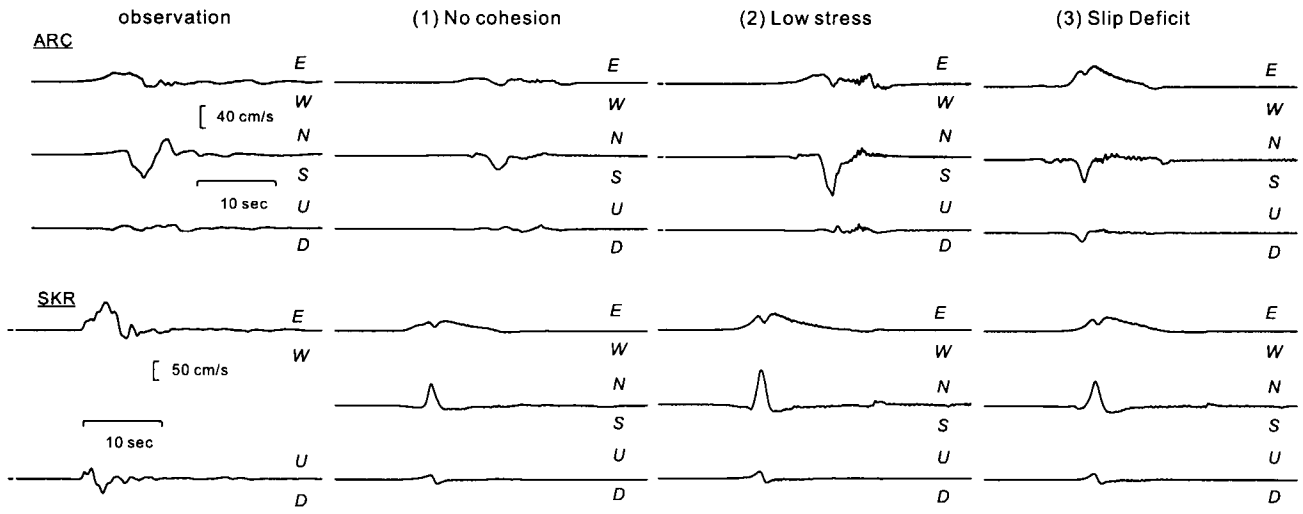

Figure 12. Comparison of synthetic seismograms at stations ARC and SKR for fault model B with different scenarios. (a) The observed seismograms. (b) The case of no cohesive force ($\sigma_0 = 0$ MPa), (c) slower rupture velocity under low stress accumulation ($R = 0.5$), and (c) heterogeneous stress loading considering previous history (Fig. 13). All of the seismograms are filtered by a low-pass filter up to 1 Hz.

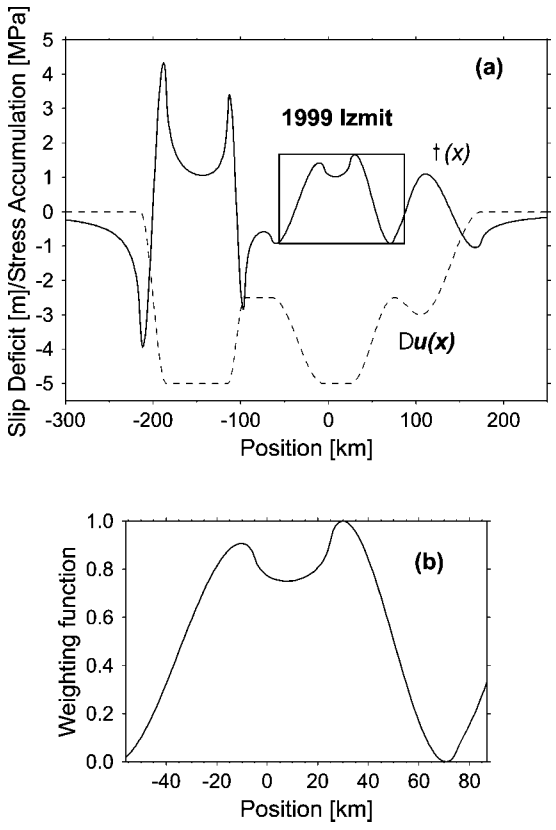

Figure 13. (a) Slip deficit just before the 1999 İzmit earthquake along the North Anatolian fault (dashed curve), which is simplified after Barka *et al.* (2002), and stress accumulation calculated as a 2D in-plane problem (solid curve). (b) Weighting function given to the parameter R.

(5). We have to note that spatial patterns of stress concentration at short scales strongly depend on the shape of the slip function and that previous events are not uniquely determined yet. What Figure 13 tells us is just that stress concentration may decrease at both ends of the İzmit earthquake because of previous events.

We introduce heterogeneous external forces σ_1 and σ_3 using this $\tau(x)$ as a weighting function (Fig. 13b) for the parameter R in equation (A5). We adopt fault model B as an example and let all the other parameters be the same as in the reference case (Fig. 5b and the left column of Fig. 11). Figures 11d and 12d present snapshots of rupture propagation and near-field synthetic seismograms, respectively. Since stress accumulation is not maximum around the hypocenter on segment IS, the rupture velocity is slow as in the low-stress case of Figure 11c. Then rupture decelerates gradually in the western part and arrests spontaneously. The arrest of rupture to the eastern direction still can be explained both by the change of strike and heterogeneous stress loading. In this way, the slip deficit can reasonably explain the size of the rupture area. However, we implicitly gave the maximum size of rupture area when we proposed the fault model of Figure 1. Therefore slip deficit should be very important for assessing future earthquakes, but it is not so important within this study.

Summary

We simulated dynamic rupture propagation along several fault geometry models and compared synthetic near-field seismograms for the 1999 İzmit earthquake. As we discussed, near-field strong motion is strongly influenced by

details of the rupture progress, which are in turn influenced by small differences in fault geometry. Numerical simulation results tell us that it is important to construct a proper fault geometry in order to reproduce strong ground motion. For example, it is desirable to interpret the unknown part under Sapanca Lake as a small bend between segments IS and SA, not as a significant jog.

We did not aim to obtain the best fault model in this study, but it should be some combination of fault models B and C from both geodetic and seismological data. At the same time, we saw that strong fault segmentations as in fault model E strongly controlled the observed surface slip. This implies that the fault geometry must be more complex near the surface, even if at depth the rupture of the İzmit earthquake is closer to that of models B and C. This discrepancy between shallow and deep behavior is discussed in Aochi (2003) through numerical simulation of a partially branched fault.

On the other hand, we provide an important constraint to explain the observed large slip near the surface. Although the free surface generally enhances the rupture on the surface in the mechanical sense, this does not work in the case where fault strength is zero on the surface and is maximum at depth. Therefore some finite fault strength is required near the surface, that is, some stress accumulation and release in the very shallow crust is necessary to explain observations. We have to investigate other earthquakes for future work, in order to discuss whether this is a general feature in the crust and whether this is also common for dipping faults.

The numerical procedure developed for this study is appropriate to understand earthquake dynamics and seismic-wave generation in geometrically complex and realistic faults. We simulated spontaneous dynamic rupture propagation along a nonplanar fault system using a BIEM and then calculated seismic-wave propagation using a FDM based on the former simulation. In this framework, we can discuss the entire process of an earthquake, including fault geometry, the tectonic stress field, and frictional fault properties.

Acknowledgments

We greatly thank M. Bouchon, who provided many valuable comments on seismological data and interpretation of the simulation results. Discussion with J.-P. Avouac and E. Durukal and their suggestions were also very useful to the progress of this work and improved this article. H. S. Akyüz, B. Delouis, and Y. Yagi as well as M. Bouchon and J.-P. Avouac showed us their numerical data and results for helping our discussions. We also thank R. Harris, and an anonymous reviewer, and D. D. Oglesby for their reviews. An author (H. A.) was supported by Centre National de la Recherche Scientifique, France, and this work is supported by project "Rupture et changement d'échelle" of ACI Catastrophes Naturelles of the Ministère de la Recherche, France. The numerical simulations were run on parallel computers at the Laboratoire de Géologie de l'Ecole Normale Supérieure Paris, France, and at the Département de Simulation Physique et Numérique de l'Institut de Physique du Globe de Paris, France.

References

Aagaard, B. T., T. H. Heaton, and J. F. Hall (2001). Dynamic earthquake rupture in the presence of lithostatic normal stress: implications for friction models and heat production, *Bull. Seism. Soc. Am.* **91,** 1763–1796.

Aochi, H. (2003). The role of fault geometry in numerical simulation of earthquake rupture, *Bull. Earthquake Res. Inst. Univ. Tokyo* (submitted for publication).

Aochi, H., and E. Fukuyama (2002). Three dimensional non-planar simulation of the 1992 Landers earthquake, *J. Geophys. Res.* **107** (B2), 10.1029/2000JB000061.

Aochi, H., E. Fukuyama, and R. Madariaga (2003). Constraints of fault constitutive parameters inferred from non-planar fault modeling, *Geochem. Geophys. Geosys.* 10. 1029/2001GC 000207.

Aochi, H., E. Fukuyama, and M. Matsu'ura (2000). Spontaneous rupture propagation on a non-planar fault in 3D elastic medium, *Pageoph* **157,** 2003–2027.

Aochi, H., R. Madariaga, and E. Fukuyama (2002). Effect of normal stress during rupture propagation along non-planar fault, *J. Geophys. Res.* **107** (B2), 10.1029/2001JB000500.

Arpat, E. (1999). *Preliminary evaluation of August 17, 1999 Kocaeli Earthquake from the Geological Field Data*, Kandilli Observatory and Earthquake Research Institute, Istanbul, Turkey.

Ayhan, M. E., C. Demir, O. Lenk, A. Kiliçoglu, Y. Altiner, A. A. Barka, S. Ergintav, and H. Özener (2002). Interseismic strain accumulation in the Marmara Sea region, *Bull. Seism. Soc. Am.* **92,** 216–229.

Barka, A., H. S. Akyüz, E. Altunel, G. Sunal, Z. Çakir, A. Dikbas, B. Yerli, R. Armijo, B. Meyer, J. B. de Chabalier, T. Rockwell, J. R. Dolan, R. Hartleb, T. Dawson, S. Christofferson, A. Tucker, T. Fumal, R. Langridge, H. Stenner, W. Lettis, J. Bachhuber, and W. Page (2002). The surface rupture and slip distribution of the August 17, 1999 İzmit earthquake, *M* 7.4, North Anatolian Fault, *Bull. Seism. Soc. Am.* **92,** 43–60.

Bouchon, M., N. Toksöz, H. Karabulut, M.-P. Bouin, M. Dieterich, M. Aktar, and M. Edie (2000). Seismic imaging of the 1999 İzmit (Turkey) rupture inferred from the near-fault recordings, *Geophys. Res. Lett.* **27,** 3013–3016.

Bouchon, M., N. Toksöz, H. Karabulut, M.-P. Bouin, M. Dieterich, M. Aktar, and M. Edie (2002). Space and time evolution of rupture and faulting during the 1999 İzmit (Turkey) earthquake, *Bull. Seism. Soc. Am.* **92,** 256–266.

Cochard, A., and R. Madariaga (1994). Dynamic faulting under rate-dependent friction, *Pageoph* **142,** 419–445.

Collino, F., and C. Tsogka (2001). Application of the perfectly matched absorbing layer model to the linear elastodynamic problem in anisotropic heterogeneous media, *Geophysics* **66,** 294–307.

Das, S., and K. Aki (1977). A numerical study of two-dimensional spontaneous rupture propagation, *Geophys. J. R. Astr. Soc.* **50,** 643–668.

Delouis, B., D. Giardini, P. Lundgren, and J. Salichon (2002). Joint inversion of InSAR, GPS, teleseismic, and strong-motion data for spatial and temporal distribution of earthquake slip: application to the 1999 İzmit mainshock, *Bull. Seism. Soc. Am.* **92,** 278–299.

Delouis, B., P. Lundgren, J. Salichon, and D. Giardini (2000). Joint inversion of InSAR and teleseismic data for the slip history of the 1999 İzmit (Turkey) earthquake, *Geophys. Res. Lett.* **27,** 3389–3392.

Fukuyama, E., and R. Madariaga (1995). Integral equation method for planar crack with arbitrary shape in 3D elastic medium, *Bull. Seism. Soc. Am.* **85,** 614–628.

Fukuyama, E., and R. Madariaga (1998). Rupture dynamics of a planar fault in a 3D elastic medium: rate- and slip-weakening friction, *Bull. Seism. Soc. Am.* **88,** 1–17.

Fukuyama, E., C. Hashimoto, and M. Matsu'ura (2002). Simulation of the transition of earthquake rupture from quasi-static growth to dynamic propagation, *Pageoph* **159,** 2057–2066.

Guatteri, M., and P. Spudich (2000). What can strong-motion data tell us

about slip-weakening fault-friction laws? *Bull. Seism. Soc. Am.* **90,** 98–116.

Harris, R. A., and S. Day (1999). Dynamic 3D simulations of earthquakes on en echelon faults, *Geophys. Res. Lett.* **26,** 2089–2092.

Harris, R. A., J. F. Dolan, R. Hartleb, and S. M. Day (2002). The 1999 İzmit, Turkey earthquake: a 3D dynamic stress transfer model of intra-earthquake triggering, *Bull. Seism. Soc. Am.* **92,** 245–255.

Hashimoto, C., and M. Matsu'ura (2002). 3-D simulation of earthquake generation cycles and evolution of fault constitutive properties, *Pageoph* **159,** 2175–2199.

Heaton, T. H. (1990). Evidence for and implications of self-healing pulses of slip in earthquake rupture, *Phys. Earth Planet. Interiors* **64,** 1–20.

Hubert-Ferrari, A., A. Barka, E. Jacques, S. Nalbant, B. Meyer, R. Armijo, P. Tapponnier, and G. C. P. King (2000). Seismic hazard in the Marmara Sea following the 17 August 1999 İzmit earthquake, *Nature* **404,** 269–272.

Ida, Y. (1972). Cohesive force across the tip of a longitudinal-shear crack and Griffith's specific surface energy, *J. Geophys. Res.* **77,** 3796–3805.

Ide, S., and M. Takeo (1997). Determination of constitutive relations of fault slip based on seismic wave analysis, *J. Geophys. Res.* **102,** 27,379–27,391.

Kame, N., and T. Yamashita (1997). Dynamic nucleation process of shallow earthquake faulting in a fault zone, *Geophys. J. Int.* **128,** 204–216.

Kame, N., and T. Yamashita (1999). Simulation of the spontaneous growth of a dynamic crack without constraints on the crack tip path, *Geophys. J. Int.* **139,** 345–358.

Kiratzi, A. A. (2002). Stress tensor inversions along the westernmost North Anatolian fault zone and its continuation into the North Aegean Sea, *Geophys. J. Int.* **151,** 360–376.

Lettis, W., J. Bachhuber, R. Witter, C. Brankman, C. E. Randolph, A. Barka, W. D. Page, and A. Kaya (2002). Influence of releasing step-overs on surface fault rupture and fault segmentation: examples from the 17 August 1999 İzmit earthquake on the North Anatolian Fault, Turkey, *Bull. Seism. Soc. Am.* **92,** 19–42.

Madariaga, R., K. Olsen, and R. Archuleta (1998). Modeling dynamic rupture in a 3D earthquake fault model, *Bull. Seism. Soc. Am.* **88,** 1182–1197.

McClusky, S., S. Balassania, A. Barka, C. Demir, S. Erginatav, I. Georgiev, O. Gurkan, M. Hamburger, K. Hurst, H. Kahle, K. Kastens, G. Kekelidze, R. King, V. Kotzev, O. Lenk, S. Mahmoud, A. Mishin, M. Nadariya, A. Ouzounis, D. Paradissis, Y. Peter, M. Prilepin, R. Reilinger, I. Sanli, H. Seeger, A. Tealeb, M. N. Toksöz, and G. Veis (2000). Global Positioning System constraints on plate kinematics and dynamics in the eastern Mediterranean and Caucasus, *J. Geophys. Res.* **105,** 5695–5719.

Michel, R., and J.-P. Avouac (2002). Deformation due to the 17 August 1999 İzmit, Turkey, earthquake measured from SPOT images, *J. Geophys. Res.* **107** (B4), 10.1029/2001JB000262.

Nielsen, S., and R. Madariaga (2002). On the self-healing fracture mode, *Bull. Seism. Soc. Am.* (submitted for publication).

Nielsen, S., and K. B. Olsen (2000). Constraints on stress and friction from dynamic rupture models of the 1994 Northridge, California, earthquake, *Pageoph* **157,** 2029–2046.

Ohnaka, M., Y. Kuwahara, and K. Yamamoto (1987). Constitutive relations between dynamic physical parameters near a tip of the propagating slip zone during stick-slip shear failure, *Tectonophys* **144,** 109–125.

Okubo, P. G., and J. H. Dieterich (1984). Effects of physical fault properties on frictional instabilities produced on simulated faults, *J. Geophys. Res.* **89,** 5817–5827.

Olsen, K. B., R. Archuleta, and Matarese (1995). Three-dimensional simulation of a magnitude 7.75 earthquake on the San Andreas fault, *Science* **270,** 1628–1632.

Olsen, K. B., E. Fukuyama, H. Aochi, and R. Madariaga (2000). Hybrid modeling of curved fault radiation in a 3D heterogeneous medium, in *2nd ACES Workshop Proc.* Hakore, Japan, October 2000, M. Matsu'ura, K. Nakajima, and P. Mora (Editors), 343–349.

Olsen, K. B., R. Madariaga, and R. J. Archuleta (1997). Three-dimensional dynamic simulation of the 1992 Landers earthquake, *Science* **278,** 834–838.

Özalaybey, S., M. Ergin, M. Aktar, C. Tapirdamaz, F. Biçmen, and A. Yörük (2002). The 1999 İzmit earthquake sequence in Turkey: seismological and tectonic aspects, *Bull. Seism. Soc. Am.* **92,** 376–386.

Palmer, A. C., and J. R. Rice (1973). The growth of slip surfaces in the progressive failure of over-consolidated clay, *Proc. R. Soc. London A* **332,** 527–548.

Polat, O., H. Haessler, A. Cisternas, H. Philip, H. Eyidogan, M. Aktar, M. Frogneux, D. Comte, and C. Gürbüz (2002). The İzmit (Kocaeli), Turkey earthquake of 17 August 1999: previous seismicity, aftershocks, and seismotectonics, *Bull. Seism. Soc. Am.* **92,** 361–375.

Quin, H. (1990). Dynamic stress drop and rupture dynamics of the October 15, 1979 Imperial Valley, California, earthquake, *Tectonophysics* **175,** 93–117.

Reilinger, R. E., S. Ergintav, R. Bürgmann, S. McClusky, O. Lenk, A. Barka, O. Gurkan, L. Hearn, K. L. Feigl, R. Cakmak, B. Aktug, H. Ozener, and M. N. Töksoz (2000). Coseismic and postseismic fault slip for the 17 August 1999, $M = 7.5$, İzmit, Turkey earthquake, *Science* **289,** 1524–1529.

Scholz, C. H. (1988). The brittle-plastic transition and the depth of seismic faulting, *Geologische Rundschau* **77,** 319–328.

Sekiguchi, H., and T. Iwata (2002). Rupture process of the 1999 Kocaeli, Turkey, Earthquake estimated from strong-motion waveforms, *Bull. Seism. Soc. Am.* **92,** 300–311.

Spudich, P., M. Guatteri, K. Otsuki, and J. Minagawa (1998). Use of fault striations and dislocation models to infer tectonic shear stress during the 1995 Hyogo-ken Nanbu (Kobe) earthquake, *Bull. Seism. Soc. Am.* **88,** 413–427.

Stein, R. S., A. A. Barka, and J. H. Dieterich (1997). Progressive failure on the North Anatolian fault since 1939 by earthquake stress triggering, *Geophys. J. Int.* **128,** 594–604.

Tada, T., and T. Yamashita (1996). The paradox of smooth and abrupt bends in two-dimensional in-plane shear-crack mechanics, *Geophys. J. Int.* **127,** 795–800.

Tada, T., and T. Yamashita (1997). Non-hypersingular boundary integral equations for two-dimensional non-planar crack analysis, *Geophys. J. Int.* **130,** 269–282.

Tada, T., E. Fukuyama, and R. Madariaga (2000). Non-hypersingular boundary integral equations for 3-D non-planar crack dynamics, *Computational Mechanics* **25,** 613–626.

Virieux, J., and R. Madariaga (1982). Dynamic faulting studied by a finite difference method, *Bull. Seism. Soc. Am.* **72,** 345–369.

Wright, T., E. Fielding, and B. Parsons (2001). Triggered slip: observations of the 17 August 1999 İzmit (Turkey) earthquake using radar interferometry, *Geophys. Res. Lett.* **28,** 1079–1082.

Yagi, Y., and M. Kikuchi (2000). Source rupture process of the Kocaeli, Turkey, earthquake of August 17, 1999, obtained by joint inversion of near-field data and teleseismic data, *Geophys. Res. Lett.* **27,** 1969–1972.

Appendix

We explain how to define the initial stress field for the given frictional parameters μ_s and μ_d in equations (3) and (4), in order to carry out the simulations. This is basically the same as the method considered in Aochi *et al.* (2002b).

The external principal stresses σ_1, σ_2, and σ_3 are unknown. We suppose that the intermediate stress σ_2 is vertical at all depths in order to permit a strike-slip movement, and it is equal to confining pressure P. Then, for simplicity, we

suppose σ_2 equal to the average of σ_1 and σ_3, that is, $P = (\sigma_1 + \sigma_3)/2$. Letting $\Delta\sigma = (\sigma_1 - \sigma_3)/2$, we can write down the principal stresses in the form

$$\sigma_1 = P + \Delta\sigma, \quad \sigma_2 = P, \quad \sigma_3 = P - \Delta\sigma. \tag{A1}$$

These external forces define the initial shear and normal stress (τ^{ini} and σ^{ini}) at each point on the fault according to the fault strike Φ:

$$\tau^{ini} = \frac{\sigma_1 - \sigma_3}{2} \sin 2\Phi = \Delta\sigma \sin 2\Phi, \tag{A2}$$

$$\sigma^{ini} = \frac{\sigma_1 + \sigma_3}{2} - \frac{\sigma_1 - \sigma_3}{2} \cos 2\Phi = P - \Delta\sigma \cos 2\Phi. \tag{A3}$$

For determining quantitatively σ_1 and σ_3 with respect to the given frictional parameters τ_p and τ_r, we also suppose the segment where the hypocenter is located, is in the most favorable direction from the viewpoint of a Coulomb-Mohr circle. σ_1 makes an angle with the first fault segment Φ_0:

$$\Phi_0 = \frac{\pi}{4} - \frac{1}{2} \tan^{-1}\mu_s. \tag{A4}$$

Then we define a parameter R, which represents the ratio of potential stress drop $\Delta\tau(=\tau^{ini} - \tau_r)$ with respect to the breakdown strength drop $\Delta\tau_b(=\tau_p - \tau_r)$ on this primary segment:

$$R = \frac{\Delta\tau}{\Delta\tau_b} = \frac{\tau^{ini} - \tau_r}{\tau_p - \tau_r}. \tag{A5}$$

Supposing the value of R, we can determine the stress difference $\Delta\sigma$, at all depths by

$$\Delta\sigma = \frac{\mu_d P + R(\sigma_0 + (\mu_s - \mu_d)P)}{\sin 2\Phi + \mu_d \cos 2\Phi + R(\mu_s - \mu_d)\cos 2\Phi}. \tag{A6}$$

With the existence of pore pressure P_H, we replace P with P_H in these equations. In the case of $\sigma_0 \neq 0$ with $P = 0$ (ground surface), $\Delta\sigma$ is still nonzero. Thus stress accumulates on the surface. On the other hand, if we take σ_0 equal to zero, $\Delta\sigma$ diminishes to zero, too.

Laboratorie de Géologie
École Normale Supérieure
24 rue Lhomond
75231 Paris Cedex 05, France

Manuscript received 1 August 2002.